nature nanotechnology

Article

https://doi.org/10.1038/s41565-024-01735-w

High-resolution three-dimensional imaging of topological textures in nanoscale single-diamond networks

Received: 9 June 2023

Accepted: 28 June 2024

Published online: 23 July 2024



D. Karpov 🖲 ^{1,2}, K. Djeghdi ^{3,4}, M. Holler 📵 ¹, S. Narjes Abdollahi 📵 ^{3,15}, K. Godlewska 📵 ³, C. Donnelly 📵 ^{5,6}, T. Yuasa 📵 ^{7,16}, H. Sai 📵 ^{7,17}, U. B. Wiesner 📵 ^{7,8},

B. D. Wilts **1**, 4.9, U. Steiner **1**, M. Musya¹⁰, S. Fukami **1**, 10,11,12,13,14

H. Ohno (10,11,12,13), I. Gunkel (10,3,4), A. Diaz (10,11,18) & J. Llandro (10,11,18)

Topological defects—extended lattice deformations that are robust against local defects and annealing—have been exploited to engineer novel properties in both hard and soft materials. Yet, their formation kinetics and nanoscale three-dimensional structure are poorly understood, impeding their benefits for nanofabrication. We describe the fabrication of a pair of topological defects in the volume of a single-diamond network (space group $Fd\bar{3}m$) templated into gold from a triblock terpolymer crystal. Using X-ray nanotomography, we resolve the three-dimensional structure of nearly 70,000 individual single-diamond unit cells with a spatial resolution of 11.2 nm, allowing analysis of the long-range order of the network. The defects observed morphologically resemble the comet and trefoil patterns of equal and opposite half-integer topological charges observed in liquid crystals. Yet our analysis of strain in the network suggests typical hard matter behaviour. Our analysis approach does not require a priori knowledge of the expected positions of the nodes in three-dimensional nanostructured systems, allowing the identification of distorted morphologies and defects in large samples.

The role of defects depends on their nature. Although point defects can alter the local material properties, extended defects involving topology can have far more profound consequences that affect the global material properties. Topological defects have been found to underpin many known physical phenomena. They can lead to new or enhanced material properties, making understanding their formation important for fundamental physics and next-generation nanotechnology¹. Research on topological defects spans both soft and hard artificial condensed matter systems. They were first extensively studied in liquid crystals² where visible light techniques can be employed. In hard condensed matter, topological defects include Dirac chains and emergent magnetic monopoles in spin ices, skyrmions, and vortices and flux tubes in superconductors³-5. Recently, topological defects and textures have

been found in the actin fibres of single-celled organisms 6 , colonies of motile bacteria 78 and nacre in bivalves 9 , where they play a critical role in development and regeneration.

An outstanding question, therefore, concerns whether mesoscale topological defects can be observed in 'bridge' systems that share biological and condensed matter properties. Soft condensed matter covers synthetic structures that combine macromolecular flexibility and formation kinetics with the periodic ordering of rigid atomic crystals. A convenient pathway to experimentally realizing soft condensed matter systems is block copolymer (BCP) self-assembly¹⁰, which offers access to a wide range of morphologies¹¹ whose properties can be tuned by the molar mass and copolymer composition and by the processing (annealing) conditions¹². Among these, three-dimensional

A full list of affiliations appears at the end of the paper. Me-mail: llandro.justin.b6@tohoku.ac.jp

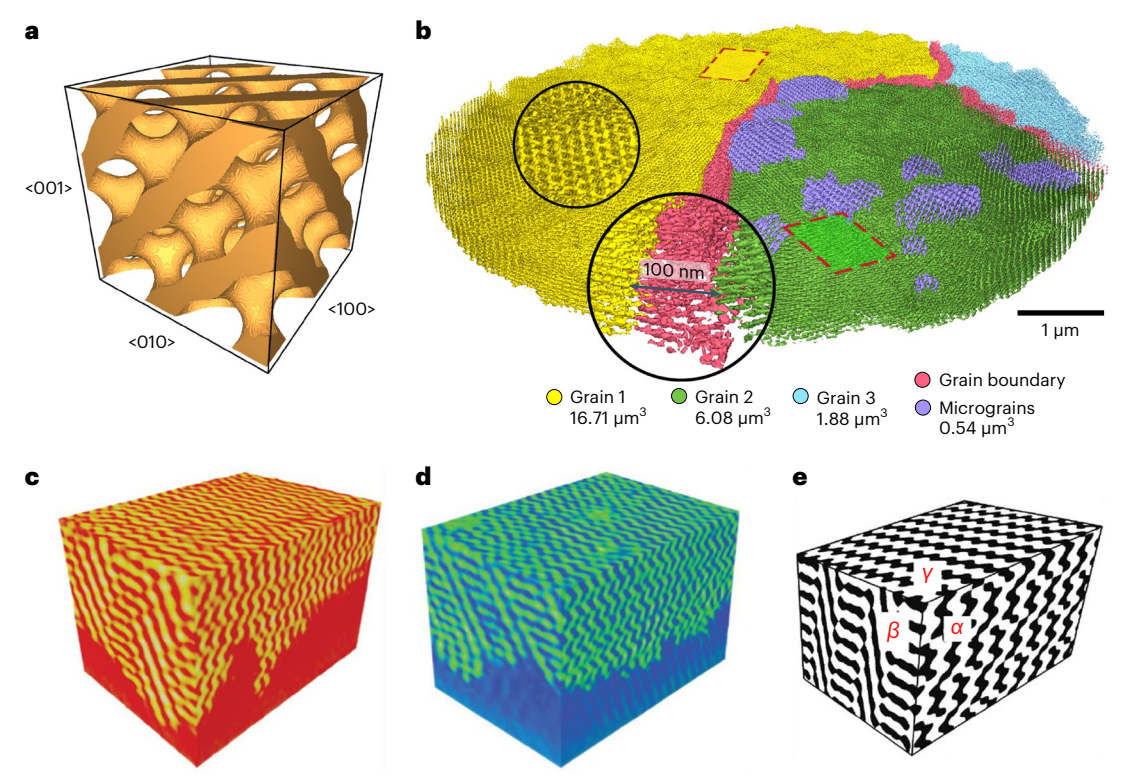


Fig. 1| **Volume rendering and identification of (multi)grain structure. a**, 3D rendering of the model structure $(2 \times 2 \times 2 \text{ unit cells})$ determined from the level-set equations for a single diamond. **b**, 3D rendering of three grains spanning the largest part of the single-diamond network, isolated micrograins near the top surface and the grain boundary. **c**, **d**, Extracted renderings from grain 1 (**c**, yellow)

and grain 2 (**d**, green) from the regions marked with dashed boxes in **b**. The two grains are oriented at 50° from each other. **e**, Matching subvolume found in the level-set generated single diamond $(647 \times 617 \times 889 \text{ nm}^3)$. The angles between the planes are $\alpha = 92^\circ$, $\beta = 77^\circ$ and $\gamma = 96^\circ$. The top plane normal vector is (0.71, 0.70, 0.03), which is approximately <110>.

(3D) ordered continuous networks 13,14 are relatively rare. A particularly well-known example is the gyroid morphology, which has attracted wide interest due to the chiral 15,16 and topological 17,18 properties of the single gyroid network of three-connected nodes formed by triads of nanowire-like struts. The single-diamond morphology 13,14 (space group $Fd\bar{3}m$), a tetrahedral network with four struts per node (see the level-set model in Fig. 1a), has also been predicted to be stable both in linear 19 and branched 20 BCPs. It has attracted enormous interest because of its potential to generate a complete photonic bandgap when it has the correct dimensions and refractive indices 20,21 . However, it has proven highly challenging to generate a single-diamond network as a well-ordered phase, even in additive-laden BCPs 22,23 . We report our observations of the single-diamond morphology templated from a neat linear BCP in a separate publication 24 .

In the current work, we observed mesoscale topological defects in an extended sample of a single-diamond network replicated from a neat BCP (triblock terpolymer) template. Using synchrotron-based hard X-ray nanotomography, we imaged a cylindrical sample 8 µm in diameter and 3 µm in height containing a 600-nm-thick layer of the single-diamond network. We achieved a 3D spatial resolution of 11.2 nm (as determined by line profiles across sharp interfaces or 7.6 nm using Fourier shell correlation). This high spatial resolution allowed us to resolve the structure of individual single-diamond unit cells (around $49 \times 75 \times 108 \text{ nm}^3$) and analyse the long-range order of the network. This long-range order analysis allowed us to identify a pair of topological defects—a 'comet'-like and a 'trefoil'-like texture—that emerged at the boundaries between diamond grains of different orientations. We confirmed the topological nature of the defects by analysing their winding number and inferred their formation mechanism by mapping distortions in the diamond network. Our analysis suggests that the topological defects emerged from the BCP/substrate interface simultaneously, thus balancing the topological charge of the system and dissipating the accumulated strain. This suggests that manipulating the substrate geometry can control the formation of mesoscale topological defects in BCP networks.

Nano-imaging over mesoscale

Three-dimensional imaging techniques are indispensable for directly observing and classifying defects in 3D nanostructured networks. Transmission electron microtomography has been successfully used to provide high-resolution 3D images²⁵⁻²⁸. However, the accessible sample volume is limited, particularly in thickness, due to the electron mean free path (typically about 100 nm; ref. 29). Alternating rounds of focused-ion beam (FIB) slicing and scanning electron microscope (SEM) imaging, known as FIB-SEM or slice-and-view SEM^{30,31}, affords an increased sample volume with a spatial resolution set by the depth of the FIB slices (as low as approximately 3 nm). However, FIB-SEM is a destructive technique, as the sample is progressively removed during imaging, meaning that subsequent measurements of the system's functionalities are not possible. On the other hand, X-ray nano-imaging techniques are both non-destructive and offer high spatial resolution^{32,33}. Here, we employed projection-based synchrotron X-ray nanotomography to non-destructively image and visualize a single-diamond network with a monoclinic unit cell (49 × 75 × 108 nm³) (ref. 24). The network was formed by self-assembly during controlled slow drying (solvent vapour annealing³⁴⁻³⁶) of films of the triblock terpolymer ISG (polyisoprene-*b*-polystyrene-*b*-poly(glycidyl methacrylate) or PI-b-PS-b-PGMA) that were initially swollen with tetrahydrofuran vapour. After forming the PI and PGMA phases into the inversion-paired networks of the alternating diamond morphology, the PI network was selectively removed by ultraviolet exposure and ethanol immersion, followed by backfilling the voided polymer template with gold by

electrodeposition. Using ptychographic X-ray computed tomography (PXCT)^{37,38}, we produced a high-resolution 3D image of the entire volume of a cylindrical micropillar sample containing approximately 70,000 unit cells of the polymer-encased Au single-diamond network. In this study, we benefitted from recent instrumentation and algorithmic advances at the cSAXS beamline of the Swiss Light Source³⁹⁻⁴², which allowed us to achieve the high spatial resolution needed to resolve the unit cells of the lattice. Detailed descriptions of sample preparation and the PXCT experiment are provided in Methods and the Supplementary Information.

Owing to the 11.2 nm spatial resolution, we were able to resolve individual unit cells and struts, analyse their connectedness and orientation in the network, quantify the distortions of the unit cells across the volume, and segment and render the grains. After data segmentation and rendering, we observed that the single-diamond network comprised individual grains of different orientations separated by boundaries (Fig. 1 and Extended Data Fig. 1). More specifically, we identified the following: (1) grain 1 (approximately 46,550 unit cells, colour-coded in yellow), (2) grain 2 (approximately 16,800 unit cells, colour-coded in green), (3) grain 3 (approximately 5,250 unit cells, colour-coded in blue), (4) micrograins (approximately 1,400 unit cells, colour-coded in purple) that formed at the top of grain 2 and (5) a grain boundary that extended throughout the fabricated sample. The cross-sectional patterns of the two largest grains (grains 1 and 2 in Fig. 1b) are consistent with the single-diamond space group, in which the nodes are connected to four neighbours. We describe in detail our analysis of the exact grain geometries in a separate publication²⁴. Both grains had the <110> crystallographic direction out-of-plane and were rotated in-plane relative to each other by approximately 50°. Extracted subvolumes from these two grains (Fig. 1c,d) were mapped onto the single-diamond level-set model (see Fig. 1e and ref. 24 for details). For the smallest grain in the fabricated sample (grain 3 in Fig. 1b), it was impossible to identify the underlying structure of the grain unambiguously. Although this was most probably due to the formation of an imperfect bicontinuous structure, either during the drying of the terpolymer template or during the metal deposition, we could not completely exclude imaging artefacts due to the position of the grain at the sample edge. A detailed discussion of the methodology for identifying grains can be found in 'Segmentation of grains' in the Supplementary Information.

Identification of topological defects

The three grains were separated by a branched grain boundary that was one to two unit cells wide (approximately spanning 100 nm, colour-coded in red in Figs. 1b and 2a). We identified two points of interest along this grain boundary as it travelled from the edge of the fabricated sample: (1) a kink in the direction of the boundary between grains 1 and 2 (marked with a red dashed box in Fig. 2b) and (2) a branching where grains 1, 2 and 3 met (marked with a blue dashed box in Fig. 2b). To better understand these features of the grain boundary and the emergence of the three grains, we present a thorough investigation of the grain geometry in the vicinity of the boundary including a detailed characterization of the overall grain topology based on a segmentation and two-dimensional (2D) slicing of the high-resolution 3D tomogram.

First, we analyse the orientation pattern of the diamond unit cell at the top surface of the grain structure (Fig. 2). Two striking textures, with their centres separated by approximately 2.7 μ m, were observed at the previously identified points of interest within the grain boundary. Morphologically, the collective orientational rearrangements gave rise to one comet-like texture (approximately 0.4 μ m by 1 μ m in size) with the 'tail' aligned approximately perpendicular to the grain boundary and one trefoil-like texture (approximately 1 μ m by 1 μ m in size) with a 120° symmetry, as schematically shown in Fig. 2d,e, respectively. Note that, from a fast Fourier transform (FFT) analysis, the peaks in

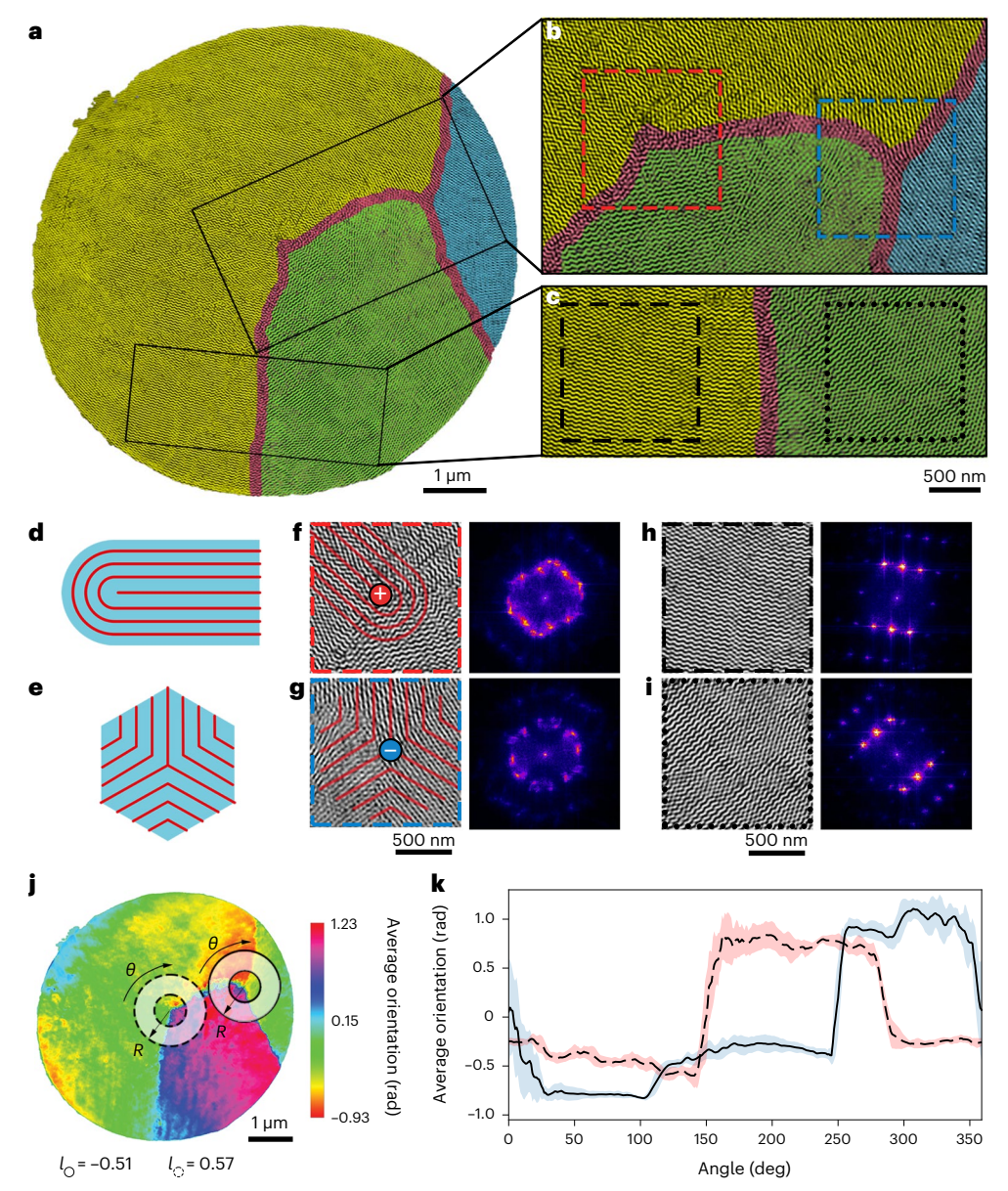
reciprocal space corresponding to the two textures were on a contour of constant radius (Fig. 2f,g) whereas those of the 'defect-free' areas of grains 1 and 2 formed a rectangular lattice corresponding to the (110) surface of its underlying approximately cubic symmetry (Fig. 2h,i). The central areas of the defect patterns therefore exhibited higher symmetry than the rest of the diamond network. The preservation of the high symmetry is characteristic of topological structures ranging from vortex cores in hard and soft condensed matter systems ⁴³ to the hypothetical cosmic strings ⁴⁴. It, thus, points to a topological nature of the textures observed in our study.

To confirm our hypothesis, we assigned a winding number to each texture by assessing the orientation changes of the struts of the diamond unit cells surrounding these defects. Note that the network was continuous across the grain boundaries and between the two topological defects, as the grains remained connected despite their different in-plane orientations. However, due to the discrete nature of the reconstruction, we defined the winding number as the radial sum (instead of an integral) over the angle θ in the vicinity of the topological defect as $l = \sum_{\theta=0^{\circ}}^{360^{\circ}} \bar{\omega}(\theta,R,z)$, where $\bar{\omega}$ is the orientation of the structures

averaged within the area ΔR (see shaded area in Fig. 2j) and over the slices of the reconstruction z. The textures show fractional winding numbers of opposite signs with l = +0.57 for the comet-like texture and l = -0.51 for the trefoil-like texture (Fig. 2i,j). The difference between the calculated values (+0.57 and -0.51) and the values expected for this kind of defect (+0.5 and -0.5) were due to local variations of the orientation, which were probably caused by averaging over the slices and the presence of local defects in the vicinity of the topological defects. It is important to note that through the approximately 230 nm thickness where the centres of topological defects can be traced, they moved by only approximately 160 nm laterally together with the grain boundary. This and the relatively small variation of the orientation between the top and the bottom interfaces suggests that the topological defects have a 2D character.

Analysis of distortion fields and strain

To understand the origins of the topological defects and how they are involved in the process of grain formation, we analysed distortions in the single-diamond network (Figs. 3 and 4). We started with a simple undistorted model structure based on the single-diamond level-set equation. We observed complex patterns when the model structure was sliced at different angles relative to the vertical axis (Extended Data Fig. 2a). When the model structure was rotated, these patterns were altered (Extended Data Fig. 2b-d). This suggested that slicing the experimental data along the vertical axis and analysing the distortion of the diamond cross-sectional patterns could be used to investigate distortions (that translate into strain) in the network. Slices 1–3 (Fig. 3d) show cross sections through the comet-like texture and then through the boundary between grains 1 (yellow grain in Fig. 1) and 2 (green grain in Fig. 1). At the texture itself, the single-diamond lattice shows distortions that propagated away from the grain boundary and appeared as a uniform bending of the diamond pattern in grain 1 and a rippling effect in grain 2. Although lattice strains are expected in solvent-annealed BCPs^{34–36}, these produce uniform compressive or shear distortions of the unit cell globally across the sample²⁴. However, for the distortions observed here, the associated strain appeared to decrease progressively with increasing distance from the defect along the boundary between grains 1 and 2 (seen as progressively reduced bending of the diamond cross-sectioned patterns in slices 1-3 in Fig. 3d), suggesting that it was associated with the presence of a topological defect, in accordance with their conventional far-field behaviour 45 rather than with a common grain boundary. Slices 5-7 show similar information for the trefoil-like defect, although the small size of grain 3 changes both the orientations and distances from the relevant defect of slices 5-7 relative to slices 1-3, making direct comparison difficult. Finally, slices 4 and 8



texture and corresponding FFT. **h**, View of highlighted area (dashed box) in **c** and corresponding FFT. **i**, View of highlighted area (dotted box) in **c** and corresponding FFT. **j**, Struts orientation map averaged over 26 slices of the tomogram, corresponding to 157 nm. The dashed circle marks a comet-like topological defect with winding number 0.57. The solid circle marks a trefoil-like topological defect with winding number –0.51. **k**, Angular dependence of the average orientation along the line plots marked by circled areas in **j**. The shading on the graph indicates one standard deviation error.

show grains 1 and 2, respectively, at a distance from the textures and grain boundary equivalent to several tens of unit cells. The distortions observed in slices 1-3 are absent in both cases.

Finally, we mapped distortion fields in the single-diamond grains by analysing the orientation of a selected cross-sectional pattern. The fringes in slice 5 in Fig. 3d are a compelling choice, as their orientation can be unambiguously segmented and mapped. Figure 4b,c shows how a rotation of the structure based on a level-set model rotated by 2° results in a substantial change in the fringe orientation from parallel to the substrate (chosen as 0° reference) to an angle of 62° with respect to the substrate. This substantial change in fringe orientation suggests a high sensitivity to distortions, with a specific fringe rotation of 62° corresponding to a 2% rotational scalar strain. We applied

this approach to the experimental data for each grain (Fig. 4d,e) to qualitatively assess the deviations from the dominant (undistorted) grain structure. We observed that the largest grain (grain 1, colour-coded as yellow in Fig. 3a) had two areas where the rotational scalar strain varied slightly between 0% and -0.93%, indicating a sub-1% distortion. This, in turn, suggested that there was a non-negligible difference in the unit-cell orientations and indicated the presence of two regions with coherent distortions within a single grain. The most distorted areas (+1.93% and -1.93%) with near 2% unit-cell distortion met at the comet-like topological texture. Moreover, Fig. 4e shows that the distortion field had a depth profile with one of the distorted regions rolling onto the other. This observation of spatial localization of two distorted regions within a single grain allowed us to infer

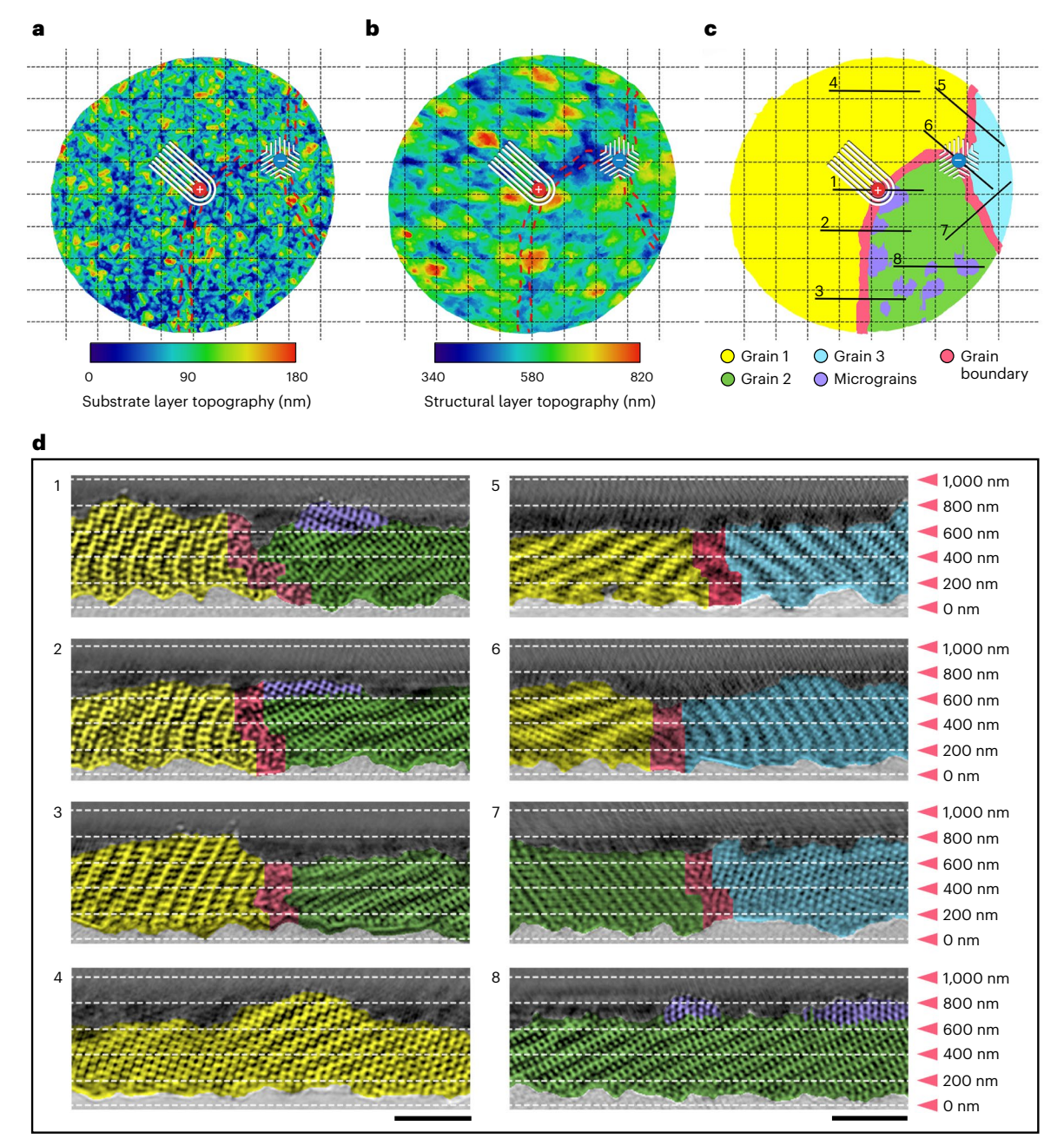


Fig. 3 | **Visualization of the topological defects inside the 3D diamond network. a**, Topography of the glass substrate, which is coated with fluorine-doped tin oxide, with marks for the locations of topological texture and the grain boundaries. **b**, Topography of the top surface of the diamond network layer with marks for the locations of topological textures and the grain boundaries.

 ${f c}$, Schematic of the grains, grain boundary and the topological textures with lines indicating the locations of the perpendicular views in ${f d}$. ${f d}$, Cross sections through the reconstructed 3D diamond network corresponding to the lines marked in ${f c}$, showing fringe patterns indicating distortion of the network. Scale bars, 500 nm.

the influence of the free surface of the single-diamond network and its interface with the substrate on the nucleation of the grains and topological textures.

In the strain maps in Fig. 4f,g, which were derived by a geometrical phase analysis⁴⁶ ('Strain analysis' in the Supplementary Information), local defects manifest as discernible discontinuities. Although the current work was focused on the observation and analysis of mesoscale topological defects spanning tens of unit cells, we also observed heterogeneity in the distribution of local defects (one to five unit cells). Specifically, the concentration of local defects increased near the grain boundary, suggesting that there was a potential correlation with the increased strain in this region. This observation is consistent with the

notion that topological defects sustain long-range structural correlations by attracting local defects through strain gradients.

From our observations, we postulated that both topological defects emerged simultaneously, thus balancing the strain produced by impinging grains. The defects, thus, act as pinning points by fixing the direction and positions of the boundaries between the grains. The comet-like texture emerged due to the two mismatched grains whereas the trefoil texture formed at the intersection of three grains. This mechanism may emerge as a method for fine-tuning the structural quality of grains, as the comet-like topology preserves long-range order in its host grains, as seen in particular from grain 1. This structural synchronization and stress-reducing property of topological defects

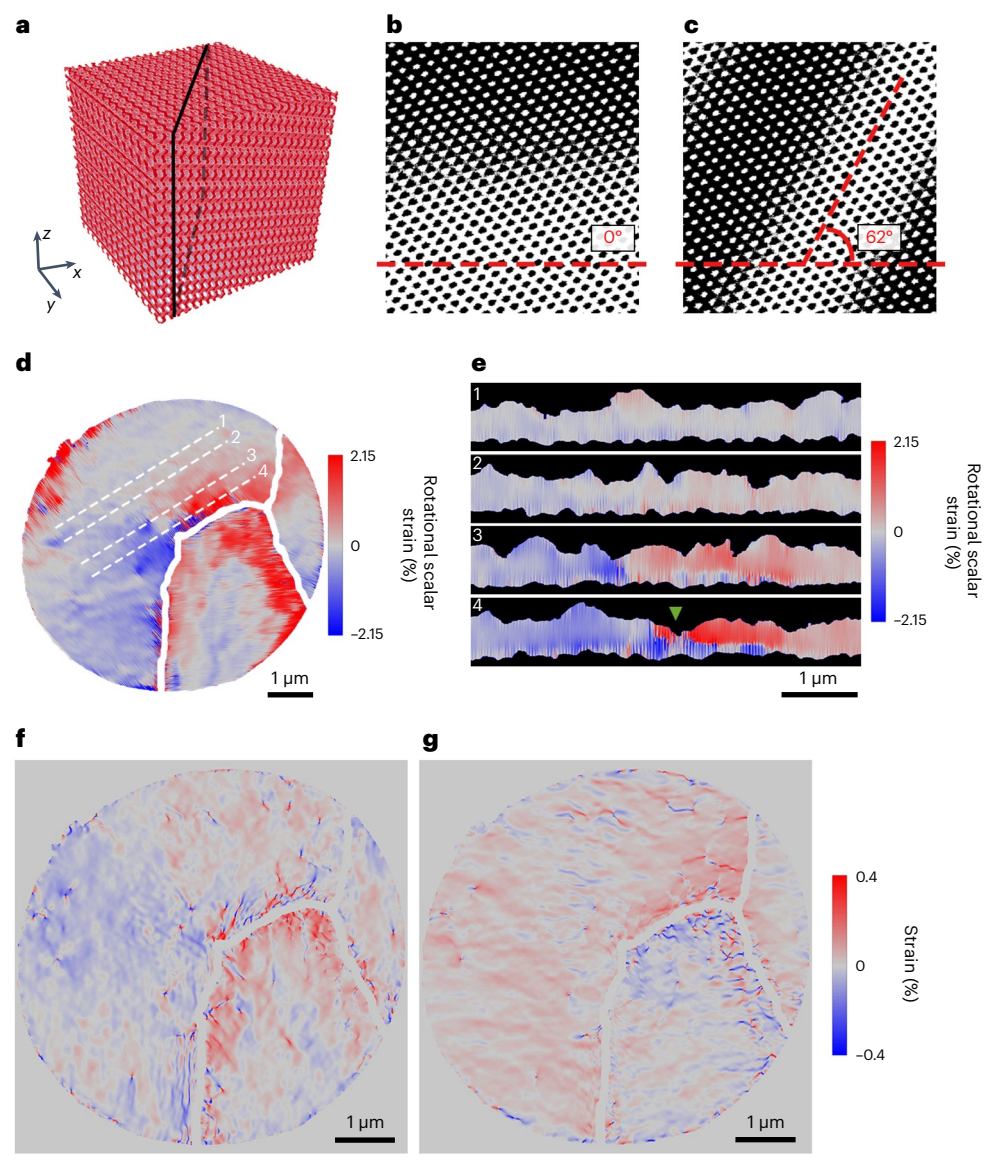


Fig. 4 | **Strain mapping. a**, 3D rendering of the model structure. **b**, Cross section through the model structure shown in **a** with a fringe at 0° orientation. **c**, Cross section through the model structure that has been rotated by 2° around the z axis. This results in a fringe rotation by 62° . **d**, Map of the rotational scalar strain obtained from the fringe orientation analysis. Dashed lines indicate the locations

of the cross-sectional views in **e**. **e**, Cross sections taken from the map of the rotational scalar strain along the lines marked in **d**. The triangle in subpanel 4 marks the location of the tail of the comet-like texture. **f**, **g**, Strain maps of ε_{xx} (**f**) and ε_{w} (**g**) obtained from the geometric phase analysis.

has previously been observed in biological systems $^{6-9}$, but this has yet to be exploited in self-assembled artificial materials.

Conclusions

Our X-ray tomography study of a large volume (about 70,000 unit cells) of a self-assembled BCP single-diamond network backfilled with Au revealed pairs of extended topological entities with subtle orientational changes over several tens of unit cells. The observed defects were cross-grain entities, centred on the grain boundary yet belonging to several grains. They differ substantially from the topological defects within individual grains previously observed in other self-assembled 3D networks 30,31,47 . At first glance, the comet-like and trefoil-like textures studied here morphologically resemble topological defects that occur in diblock copolymers such as PS-b-poly(methyl methacrylate), which forminto cylinders parallel to the substrate or substrate-perpendicular lamellae 48,49 . However, in such systems, the defects are abrupt disclinations that break across quasi-2D stripe patterns rather than collective orientational changes.

Instead, the micrometre-scale comet and trefoil in the BCPtemplated single-diamond network have more in common with analogous topological textures known from studies of nematic liquid crystals^{2,49} and recently also observed in *Hydra* single-celled organisms⁶ and colonies of motile bacteria^{7,8}. By contrast, the disclinations in cylinder-forming and lamella-forming BCPs in biological systems more closely resemble the (millimetre-scale) +1/2 and -1/2 defects in the skin on the fingertips, which occur in topological charge-conserving pairs⁵⁰. In all previously reported non-BCP systems, order is governed by a director, a modulo- π vector defined by the long axes of the rod-shaped bacteria in the colonies, the preferential local order axis of nematic molecules in liquid crystals, actin filaments in the single-celled organism Hydra and the ridges in fingerprints. Our identification of analogous defects in BCP diamonds suggests that a director may also exist in this system in the form of the strain field revealed by comparing experimental patterns with undistorted patterns from a level-set diamond model. Topological defects of the observed type can exist in the diamond network, as similar self-assembled 3D networks

in biological samples rather exhibit dislocations ⁴⁷, analogous to 'hard matter' atomic crystals.

The methodology devised in our study can be applied to future studies of topological defects in self-assembled 3D networks, both natural and synthetic. Moreover, the 3D fringe orientation analysis used in our work can be extended to other 3D periodic structures to investigate the role of displacement fields in systems for which the analytical modelling is challenging. The achieved high 3D spatial resolution combined with large sample volumes can be used to study defect formation over macroscopic distances in self-assembly processes. Gaining an understanding of defects naturally leads to the possibility of defect engineering that can realize new phenomena and improve material properties.

More fundamentally, the extended topological defects in the self-assembled system observed in our work share characteristics of synthetic (for example, liquid crystals) and biological systems. This supports the emerging consensus that topology-driven physics is one of the leading mechanisms for structure formation in soft matter stand further suggests that self-assembly can be used as a model process to investigate the role of topology in nature.

Online content

Any methods, additional references, Nature Portfolio reporting summaries, source data, extended data, supplementary information, acknowledgements, peer review information; details of author contributions and competing interests; and statements of data and code availability are available at https://doi.org/10.1038/s41565-024-01735-w.

References

- Liu, P., Williams, J. R. & Cha, J. J. Topological nanomaterials. Nat. Rev. Mater. 4, 479–496 (2019).
- Tkalec, U. et al. Reconfigurable knots and links in chiral nematic colloids. Science 333, 62–65 (2011).
- 3. Bramwell, S. T. & Harris, M. J. The history of spin ice. *J. Phys. Condens. Matter* **32**, 374010 (2020).
- Fert, A., Reyren, N. & Cros, V. Magnetic skyrmions: advances in physics and potential applications. Nat. Rev. Mater. 2, 17031 (2017).
- Sato, M. & Ando, Y. Topological superconductors: a review. Rep. Prog. Phys. 80, 076501 (2017).
- Maroudas-Sacks, Y. et al. Topological defects in the nematic order of actin fibres as organization centres of *Hydra* morphogenesis. *Nat. Phys.* 17, 251–259 (2021).
- Copenhagen, K., Alert, R., Wingreen, N. S. & Shaevitz, J. W. Topological defects promote layer formation in Myxococcus xanthus colonies. Nat. Phys. 17, 211–215 (2021).
- Meacock, O. J., Doostmohammadi, A., Foster, K. R., Yeomans, J. M. & Durham, W. M. Bacteria solve the problem of crowding by moving slowly. *Nat. Phys.* 17, 205–210 (2021).
- Beliaev, M., Zöllner, D., Pacureanu, A., Zaslansky, P. & Zlotnikov, I. Dynamics of topological defects and structural synchronization in a forming periodic tissue. *Nat. Phys.* 17, 410–415 (2021).
- Bates, F. S. & Fredrickson, G. H. Block copolymers-designer soft materials. *Phys. Today* 52, 32–38 (1999).
- Abetz, V. & Simon, P. F. W. in Block Copolymers I. Advances in Polymer Science, Vol. 189 (ed. Abetz, V.) 125–212 (Springer, 2010).
- 12. Majewski, P. W. & Yager, K. G. Rapid ordering of block copolymer thin films. *J. Phys. Condens. Matter* **28**, 403002 (2016).
- Meuler, A. J., Hillmyer, M. A. & Bates, F. S. Ordered network mesostructures in block polymer materials. *Macromolecules* 42, 7221–7250 (2009).
- 14. Thomas, E. L. Nanoscale 3D ordered polymer networks. *Sci. China Chem.* **61**, 25–32 (2018).
- Dolan, J. A. et al. Optical properties of gyroid structured materials: from photonic crystals to metamaterials. Adv. Opt. Mater. 3, 12–32 (2015).

- Wu, L., Zhang, W. & Zhang, D. Engineering gyroid-structured functional materials via templates discovered in nature and in the lab. Small 11. 5004–5022 (2015).
- Lu, L., Fu, L., Joannopoulos, J. D. & Soljačić, M. Weyl points and line nodes in gyroid photonic crystals. *Nat. Photonics* 7, 294–299 (2013).
- Lu, L. et al. Experimental observation of Weyl points. Science 349, 622–624 (2015).
- Qin, J., Bates, F. S. & Morse, D. C. Phase behavior of nonfrustrated ABC triblock copolymers: weak and intermediate segregation. *Macromolecules* 43, 5128–5136 (2010).
- Lequieu, J., Quah, T., Delaney, K. T. & Fredrickson, G. H. Complete photonic band gaps with nonfrustrated ABC bottlebrush block polymers. ACS Macro Lett. 9, 1074–1080 (2020).
- Maldovan, M. & Thomas, E. L. Diamond-structured photonic crystals. *Nat. Mater.* 3, 593–600 (2004).
- 22. La, Y. et al. Templated synthesis of cubic crystalline single networks having large open-space lattices by polymer cubosomes. *Nat. Commun.* **9**, 5327 (2018).
- Sheng, Q. et al. Self-assembly of single-diamond-surface networks. Angew. Chem. Int. Ed. 60, 15236–15242 (2021).
- 24. Djeghdi, K. et al. X-ray nanotomography reveals formation of single diamonds by block copolymer self-assembly. Preprint at https://arxiv.org/abs/2304.12027 (2023).
- Spontak, R. J. et al. Phase behavior of ordered diblock copolymer blends: effect of compositional heterogeneity. *Macromolecules* 29, 4494–4507 (1996).
- Jinnai, H. et al. Direct measurement of interfacial curvature distributions in a bicontinuous block copolymer morphology. *Phys. Rev. Lett.* 84, 518–521 (2000).
- 27. Jinnai, H., Kajihara, T., Watashiba, H., Nishikawa, Y. & Spontak, R. J. Interfacial and topological measurements of bicontinuous polymer morphologies. *Phys. Rev. E* **64**, 010803 (2001).
- 28. Li, Z. et al. Linking experiment and theory for three-dimensional networked binary metal nanoparticle–triblock terpolymer superstructures. *Nat. Commun.* **5**, 3247 (2014).
- 29. Yan, H., Voorhees, P. W. & Xin, H. L. Nanoscale X-ray and electron tomography. MRS Bull. 45, 264–271 (2020).
- Feng, X., Guo, H. & Thomas, E. L. Topological defects in tubular network block copolymers. *Polymer* 168, 44–52 (2019).
- 31. Feng, X. et al. Seeing mesoatomic distortions in soft-matter crystals of a double-gyroid block copolymer. *Nature* **575**, 175–179 (2019).
- Michelson, A. et al. Three-dimensional visualization of nanoparticle lattices and multimaterial frameworks. Science 376, 203–207 (2022).
- 33. Rana, A. et al. Three-dimensional topological magnetic monopoles and their interactions in a ferromagnetic meta-lattice. *Nat. Nanotechnol.* **18**, 227–232 (2023).
- 34. Kim, S. H., Misner, M. J., Xu, T., Kimura, M. & Russell, T. P. Highly oriented and ordered arrays from block copolymers via solvent evaporation. *Adv. Mater.* **16**, 226–231 (2004).
- Sinturel, C., Vayer, M., Morris, M. & Hillmyer, M. A. Solvent vapor annealing of block polymer thin films. *Macromolecules* 46, 5399–5415 (2013).
- 36. Dolan, J. A. et al. Controlling self-assembly in gyroid terpolymer films by solvent vapor annealing. *Small* **14**, 1802401 (2018).
- 37. Dierolf, M. et al. Ptychographic X-ray computed tomography at the nanoscale. *Nature* **467**, 436–439 (2010).
- 38. Pfeiffer, F. X-ray ptychography. Nat. Photonics 12, 9-17 (2018).
- 39. Holler, M. et al. X-ray ptychographic computed tomography at 16 nm isotropic 3D resolution. *Sci. Rep.* **4**, 3857 (2014).
- Holler, M. et al. High-resolution non-destructive three-dimensional imaging of integrated circuits. *Nature* 543, 402–406 (2017).

- 41. Wilts, B. D. et al. Evolutionary-optimized photonic network structure in white beetle wing scales. *Adv. Mater.* **30**, 1702057 (2017).
- Donnelly, C. et al. Three-dimensional magnetization structures revealed with X-ray vector nanotomography. *Nature* 547, 328–331 (2017).
- Teo, J. C. Y. & Hughes, T. L. Topological defects in symmetry-protected topological phases. *Annu. Rev. Condens. Matter Phys.* 8, 211–237 (2017).
- 44. Kibble, T. W. B. Topology of cosmic domains and strings. *J. Phys. A* **9**, 1387–1398 (1976).
- Chaikin, P. & Lubensky, T. in *Principles of Condensed Matter Physics* (eds Chaikin, P. M. et al.) 495–589 (Cambridge Univ. Press, 1995).
- Hÿtch, M. J., Snoeck, E. & Kilaas, R. Quantitative measurement of displacement and strain fields from HREM micrographs. *Ultramicroscopy* 74, 131–146 (1998).
- 47. Singer, A. et al. Domain morphology, boundaries, and topological defects in biophotonic gyroid nanostructures of butterfly wing scales. Sci. Adv. 2, e1600149 (2016).
- Li, W.-H. & Müller, M. Defects in the self-assembly of block copolymers and their relevance for directed self-assembly. *Annu. Rev. Chem. Biomol. Eng.* 6, 187–216 (2015).

- Jangizehi, A., Schmid, F., Besenius, P., Kremer, K. & Seiffert, S. Defects and defect engineering in soft matter. Soft Matter 16, 10809–10859 (2020).
- Penrose, L. S. Dermatoglyphic topology. *Nature* **205**, 544–546 (1965).
- 51. Serra, F., Tkalec, U. & Lopez-Leon, T. Editorial: topological soft matter. *Front. Phys.* **8**, 373 (2020).

Publisher's note Springer Nature remains neutral with regard to jurisdictional claims in published maps and institutional affiliations.

Springer Nature or its licensor (e.g. a society or other partner) holds exclusive rights to this article under a publishing agreement with the author(s) or other rightsholder(s); author self-archiving of the accepted manuscript version of this article is solely governed by the terms of such publishing agreement and applicable law.

© The Author(s), under exclusive licence to Springer Nature Limited 2024

¹Paul Scherrer Institute, Villigen, Switzerland. ²European Synchrotron Radiation Facility, Grenoble, France. ³Adolphe Merkle Institute, University of Fribourg, Fribourg, Fribourg, Switzerland. ⁴Swiss National Center of Competence in Research Bio-Inspired Materials, University of Fribourg, Fribourg, Switzerland. ⁵Max Planck Institute for Chemical Physics of Solids, Dresden, Germany. ⁶International Institute for Sustainability with Knotted Chiral Meta Matter (WPI-SKCM2), Hiroshima University, Hiroshima, Japan. ⁷Department of Materials Science and Engineering, Cornell University, Ithaca, NY, USA. ⁸Kavli Institute at Cornell for Nanoscale Science, Cornell University, Ithaca, NY, USA. ⁹Department of Chemistry and Physics of Materials, University of Salzburg, Salzburg, Austria. ¹⁰Laboratory for Nanoelectronics and Spintronics, Research Institute of Electrical Communication, Tohoku University, Sendai, Japan. ¹¹Center for Science and Innovation in Spintronics, Tohoku University, Sendai, Japan. ¹²Center for Innovative Integrated Electronic Systems, Tohoku University, Sendai, Japan. ¹³WPI Advanced Institute for Materials Research, Tohoku University, Sendai, Japan. ¹⁴Inamori Research Institute for Science, Kyoto, Japan. ¹⁵Present address: Department of Chemistry, University of Basel, Basel, Switzerland. ¹⁶Present address: Yokkaichi Research Center, JSR Corporation, Yokkaichi, Japan. ¹⁷Present address: Simpson Querrey Institute for Bionanotechnology, Northwestern University, Evanston, IL, USA. ¹⁸Present address: Sumitomo Chemical Co., Ltd, Tokyo, Japan. —e-mail: llandro.justin.b6@tohoku.ac.jp

Methods

Sample preparation

Films of a nanostructured 3D diamond morphology were prepared as detailed in the Supplementary Information by self-assembly of the triblock terpolymer ISG under solvent vapour annealing. The number average molar mass M_n of ISG was 67.4 kg mol⁻¹, and its polydispersity index was 1.08. The volume fractions were $f_{\rm Pl} = 0.29$, $f_{\rm PS} = 0.52$ and $f_{\rm PGMA} = 0.19$, as described elsewhere²⁴. The resulting PI diamond minority network was selectively removed from the ISG terpolymer film by ultraviolet exposure and ethanol immersion, followed by backfilling of the voided network space with gold by electrodeposition. The polymer-encased Au single-diamond film thus formed was around 600 nm thick, and its unit cell had a monoclinic lattice distortion²⁴.

To study the nanoscale morphology of the diamond network, we extracted a pillar 8 μ m in diameter that contained the single-diamond layer from the substrate and transferred it onto a custom sample mounting pin (Extended Data Fig. 3 and 'Micropillar fabrication by focused ion beam' in the Supplementary Information).

Data acquisition and tomographic reconstruction

The experiment was performed at the cSAXS beamline of the Swiss Light Source using the flexible tomography nano-imaging end station (Extended Data Fig. 4)^{39,40}. The 2D projections of the sample were obtained using X-ray ptychography³⁸. In this imaging technique, the sample is raster scanned with a monochromatic and spatially coherent focused X-ray beam in a manner that guarantees a partial overlap between adjacent illuminated areas. The beam scatters from each scanned point on the sample and the resulting diffraction patterns are collected in transmission in the far field by an area detector. The recorded diffraction patterns are then iteratively inverted into real-space images with quantitative phase and absorption contrast using phase retrieval algorithms ^{38,52}. Instrumental characteristics such as detector noise and vibrations of the sample will contribute to a loss of resolution, as in other imaging techniques. However, in X-ray ptychography, the absence of a physical imaging lens allows the recovery of high-resolution information that is aberration-free and, in theory, limited only by the X-ray wavelength and the acceptance angle of the detector rather than the size of the illumination or scanning steps.

Two-dimensional ptychographic images acquired at different rotation angles of the sample were used for the final tomographic reconstruction of the sample volume. This extension of X-ray ptvchography to 3D is PXCT^{37,38}. In recent years, PXCT has found diverse applications such as the non-destructive imaging of integrated circuits⁴⁰, biophotonic structures⁴¹ and magnetization structures⁴². It can achieve a resolution in 3D of 14.6 nm (ref. 40). In our measurements, we demonstrated that PXCT can achieve a uniform 3D spatial resolution of 11.2 nm (as determined by line profiles across sharp interfaces or 7.6 nm using Fourier shell correlation; Extended Data Fig. 5), which was sufficient for visualizing the structure of the individual single-diamond unit cells. To reconstruct the volume of the 8-µm-diameter and 600-nm-thick Au single-diamond layer in the sample, we acquired 2,400 projections of the sample equally spaced over an angular range of 180°. The measurement of a single projection took about 50 s, resulting in 35 h for the high-resolution tomogram. We estimated that a dose of about 1×10^{10} Gy was delivered to the sample during the measurement.

More details about the PXCT measurement and the real-space reconstruction of the Au single-diamond network in 3D as well as implications for low-contrast samples can be found in 'Consideration for low-contrast samples' in the Supplementary Information.

Data availability

The raw data supporting the findings of this study are permanently deposited at the Paul Scherrer Institute repository and can be accessed from http://doi.psi.ch/detail/10.16907/409237cf-63de-43ca-b525-a68025a93d63. The derived data, including the

reconstructed ptychographic projections and the reconstructed tomogram, are available at the same repository and can be accessed from http://doi.psi.ch/detail/10.16907/a961ab58-de00-40b4-ad6c-bc096776c476. Further details and any other data related to this study are available from the corresponding author upon reasonable request.

Code availability

The code for data reconstruction is available for download directly from cSAXS beamline pages https://www.psi.ch/en/sls/csaxs/software. The package with input/output functions can be downloaded from 'cSAXS beamline software packages: Base package'. The package for ptychographic reconstruction can be downloaded from 'cSAXS beamline software packages: PtychoShelves'. The package for tomographic reconstruction can be downloaded from 'cSAXS beamline software packages: Tomography package'.

References

52. Rodenburg, J. M. & Faulkner, H. M. L. A phase retrieval algorithm for shifting illumination. *Appl. Phys. Lett.* **85**, 4795–4797 (2004).

Acknowledgements

This study was financially supported by the Swiss National Science Foundation (Grant Nos. 163220, 188647, 168223 and 190467) and the National Center of Competence in Research Bio-Inspired Materials (Grant No. 51NF40-182881). This project also received funding from the European Union's Horizon 2020 research and innovation programme (Marie Sklodowska-Curie Grant Agreement No. 706329/cOMPoSe to I.G.). This work was also funded by the European Soft Matter Infrastructure (Grant Agreement No. 731019/EUSMI to J.L. and D.K.) and made use of the Cornell Center for Materials Research Shared Facilities supported by the National Science Foundation's Materials Research Science and Engineering Centers programme (Grant No. DMR-1719875). U.B.W. thanks the National Science Foundation for financial support (Grant No. DMR-2307013). D.K. acknowledges funding from the Swiss National Science Foundation (Grant No. 200021 175905). J.L. and S.F. acknowledge support from the Japan Society for the Promotion of Science (KAKENHI Grant Nos. 21KO4816, 24H00039 and 24H02235), Cooperative Research Projects of the Center for Science and Innovation in Spintronics at Tohoku University and the Graduate Program for Spintronics at Tohoku University. C.D. acknowledges support from the Max Planck Society's Lise Meitner Excellence Program and funding from the European Research Council (Starting Grant No. 3DNANOQUANT 101116043). U.S. acknowledges funding from the Adolphe Merkle Foundation and the European Research Council (Advanced Grant No. PrISMoID 833895). We further acknowledge the Paul Scherrer Institut, Villigen, Switzerland, for providing synchrotron radiation beamtime at beamline X12SA (cSAXS) of the Swiss Light Source.

Author contributions

J.L., D.K., A.D. and I.G. conceived the study and supervised the research, with assistance from B.D.W., U.S., S.F. and H.O. The terpolymer was synthesized by T.Y. and H.S. under the supervision of U.B.W. The solvent annealing set-up was designed and built by I.G. and B.D.W. The solvent annealing protocol was developed by K.G. under the supervision of I.G. The polymer template and the gold replica were prepared by S.N.A. The micropillar sample was prepared by M.M. under the supervision of J.L., S.F. and H.O. The PXCT experiment was performed by D.K., M.H., C.D., A.D. and J.L. The ptychographic and tomographic reconstruction was performed by A.D. and D.K. Image processing, domain segmentation and topological charge analysis were performed by D.K. with

assistance from K.D., J.L. and I.G. Local structure analysis and structure identification were performed by K.D. The strain analysis was performed by D.K. The manuscript was written by D.K. and J.L. with contributions from all authors, including feedback on results, analysis and interpretation.

Competing interests

The authors declare no competing interests.

Additional information

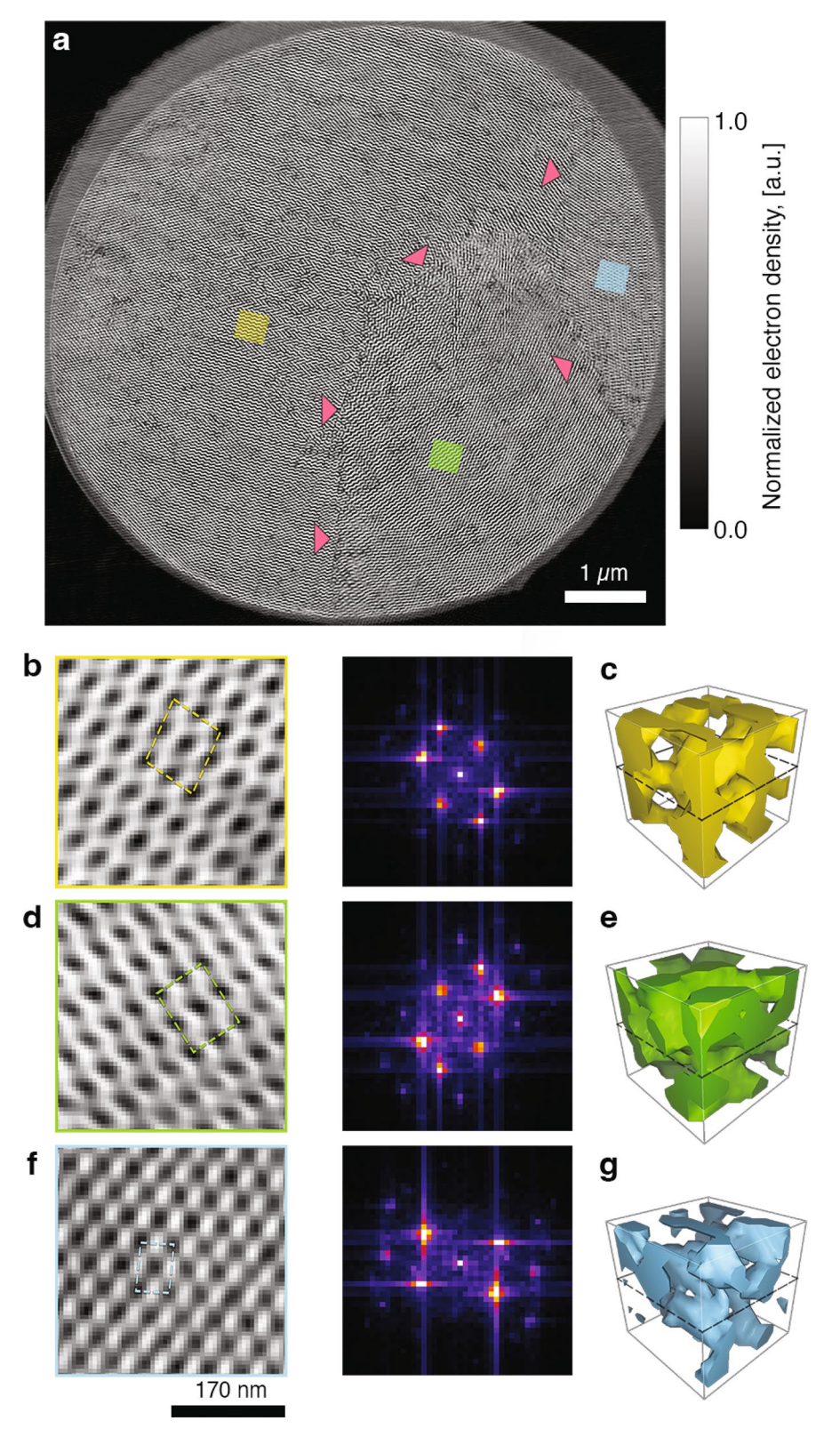
Extended data is available for this paper at https://doi.org/10.1038/s41565-024-01735-w.

Supplementary information The online version contains supplementary material available at https://doi.org/10.1038/s41565-024-01735-w.

Correspondence and requests for materials should be addressed to J. Llandro.

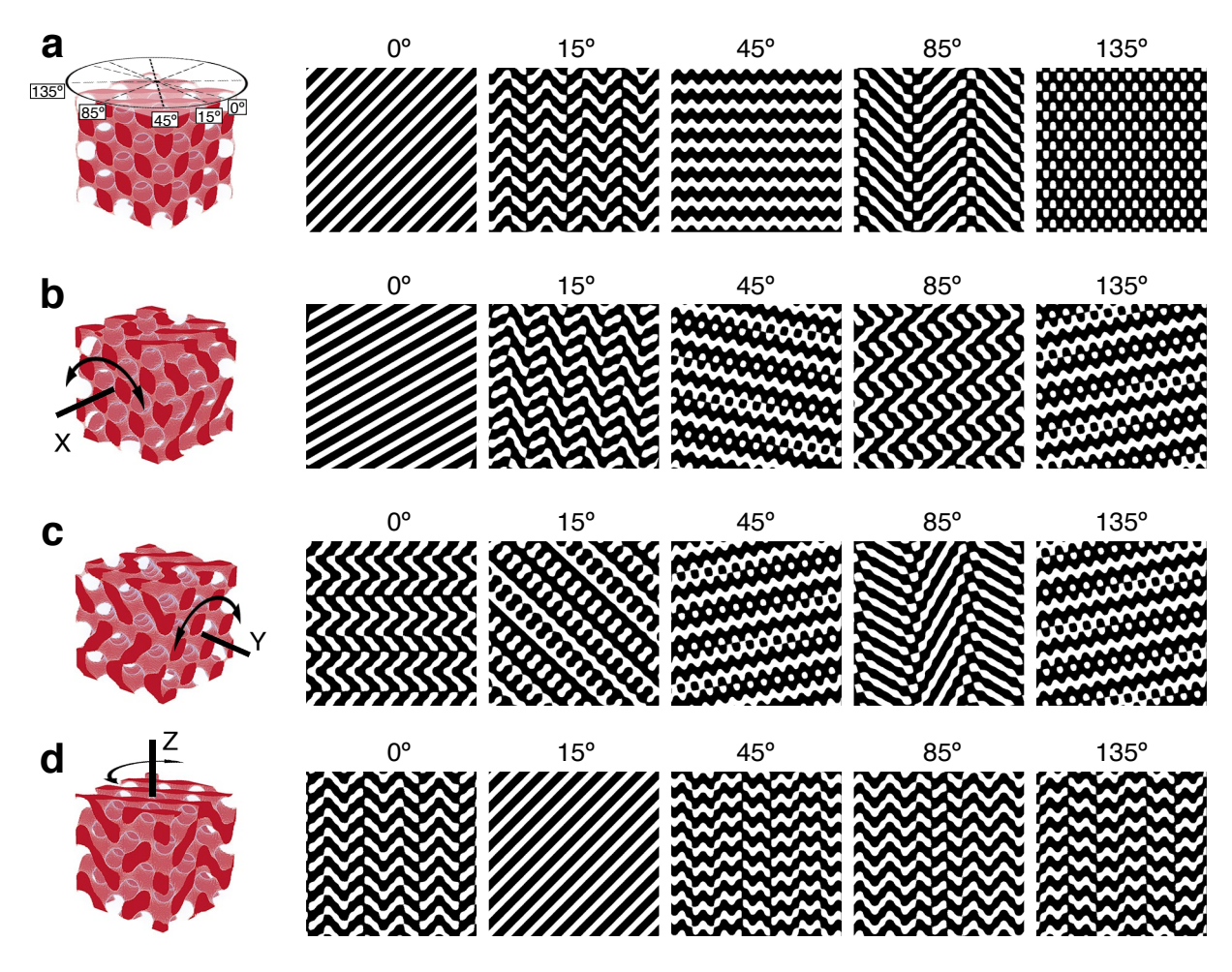
Peer review information *Nature Nanotechnology* thanks Suzana Nunes and the other, anonymous, reviewer(s) for their contribution to the peer review of this work.

Reprints and permissions information is available at www.nature.com/reprints.



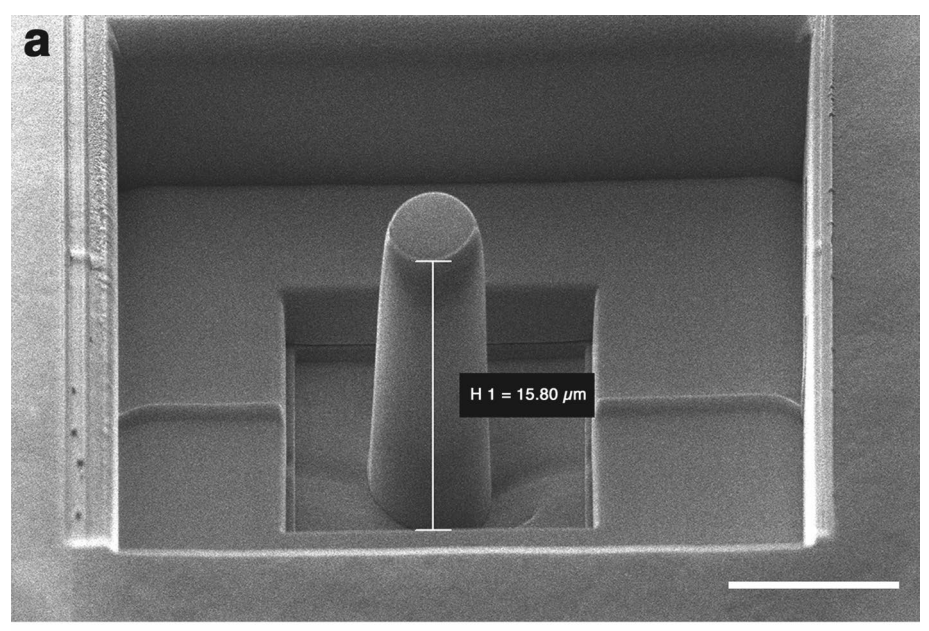
Extended Data Fig. 1 | Rendering of 2x2x2 unit cell volumes within individual grains. (a) A slice through the volume (parallel to the substrate) indicating the grain boundary with triangular marks. (b) Slice through the yellow grain perpendicular to the sample surface and its Fourier transform. (c) 3D rendering of the small volume marked with a rectangle in \mathbf{b} . (d) Slice through the green

grain perpendicular to the sample surface and its Fourier transform. (\boldsymbol{e}) 3D rendering of the small volume marked with a rectangle in \boldsymbol{d} . (\boldsymbol{f}) Slice through the blue grain perpendicular to the sample surface and its Fourier transform. (\boldsymbol{g}) 3D rendering of the small volume marked with a rectangle in \boldsymbol{f} .



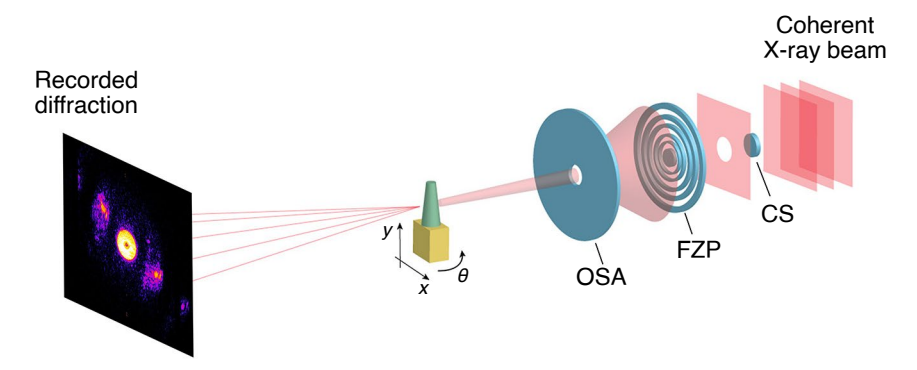
Extended Data Fig. 2 | Changes to the stripe patterns that result from rotation of the model volume. (a) 3D rendering and slices through model diamond structure showing the different patterns. (b) 3D rendering and slices through the model rotated by 15° around the x-axis showing the dependence of

the patterns on rotation. (c) 3D rendering and slices through the model rotated by 15° around the y-axis showing the dependence of the patterns on rotation. (d) 3D rendering and slices through the model rotated by 15° around the z-axis showing the dependence of the patterns on rotation.





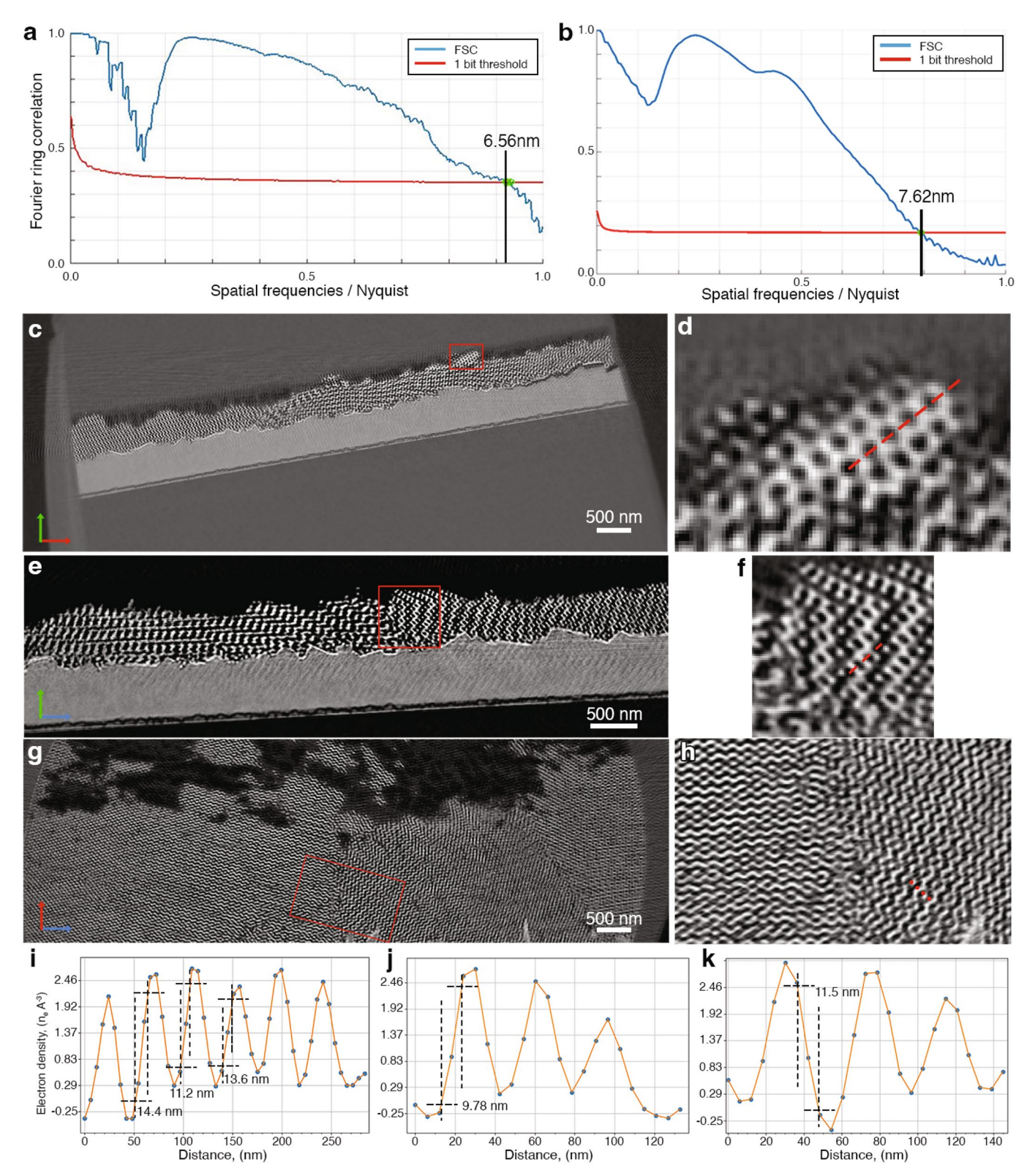
 $\textbf{Extended Data Fig. 3} | \textbf{Sample preparation by focused ion beam (FIB). (a)} \ Scanning electron \ microscopy (SEM) \ image showing the sample after FIB \ milling of its surrounding material. (b) SEM image of the micropillar sample mounted on the OMNY pin. Scale bars are 10 \ \mum.$



Extended Data Fig. 4 | Principal scheme of the ptychographic experiment.

X-rays with a high degree of coherence are focused by a Fresnel zone plate (FZP) in combination with a central stop (CS) and an order sorting aperture (OSA) to define a coherent illumination onto the sample. X-rays propagate through

the sample and are recorded by a 2D detector in the far field. The sample is scanned along x and y for ptychographic imaging, and then rotated in theta for tomographic acquisitions.



Extended Data Fig. 5 | **Evaluation of the resolution.** (a) 2D resolution estimate of a single ptychographic projection. We show the Fourier ring correlation (FRC) between two ptychographic projections acquired at the same angle as a function of the spatial frequency. The point at which the FRC intersects the threshold curve calculated according to the 1-bit criterion is used as an estimation for the resolution in 2D corresponding to each of the images. (b) 3D resolution estimate of the tomogram. We show the Fourier shell correlation (FSC) between two subtomograms, each computed with half of the available projections, as a function

of the spatial frequency. The point at which the FSC intersects a calculated threshold for the $\frac{1}{2}$ -bit criterion is an estimation of the 3D resolution of the full tomogram, using all the available projections. 2D slices through the tomogram showing (c) XZ, (e) YZ, and (g) XY planes. (d, f, h) Magnified regions are indicated by red boxes in (c, e, g), respectively. (i–k) Line profiles associated with the red dotted lines are shown in (d, f, h), respectively. The numbers indicate the width of the profile line across sharp features of the image using the 10%-90% intensity criterion.